

Bayesian optimization for re-analysis and calibration of extreme sea state events simulated with a spectral third-generation wave model

Cédric Goeury^{1,2}, Thierry Fouquet¹, Maria Teles¹, and Michel Benoit^{1,2}

¹EDF R&D, National Laboratory for Hydraulics and Environment (LNHE), 6 Quai Watier, 78400 Chatou, France

²Saint-Venant Hydraulics Laboratory, LHSV, ENPC, Institut Polytechnique de Paris, EDF R&D, 6 Quai Watier, 78400 Chatou, France

January 5, 2026

Abstract

Accurate hindcasting of extreme sea state events is essential for coastal engineering, risk assessment, and climate studies. However, the reliability of numerical wave models remains limited by uncertainties in physical parameterizations and model inputs. This study presents a novel calibration framework based on Bayesian Optimization (BO), leveraging the Tree structured Parzen Estimator (TPE) to efficiently estimate uncertain sink term parameters, specifically bottom friction dissipation, depth induced breaking, and wave dissipation from strong opposing currents, in the ANEMOC-3 hindcast wave model. The proposed method enables joint optimization of continuous parameters and discrete model structures, significantly reducing discrepancies between model outputs and observations. Applied to a one month period encompassing multiple intense storm events along the French Atlantic coast, the calibrated model demonstrates improved agreement with buoy measurements, achieving lower bias, RMSE, and scatter index relative to the default sea-state solver configuration. The results highlight the potential of BO to automate and enhance wave model calibration, offering a scalable and flexible approach applicable to a wide range of geophysical modeling problems. Future extensions include multi-objective optimization, uncertainty quantification, and integration of additional observational datasets.

1 Introduction

Accurate hindcasting of sea state conditions plays a pivotal role in marine engineering (Accensi et al., 2021; Alday and Lavidas, 2024), navigational safety (Rogers et al., 2007), and climate research (Akpinar et al., 2023). By integrating numerical wave models with atmospheric re-analysis data, hindcasting enables the generation of long-time wave datasets that are indispensable for assessing extreme events (Wurjanto et al., 2020) and characterizing operational climates (Allahdadi et al., 2019), particularly in regions with sparse observational coverage. These reconstructions not only inform the design and resilience of offshore and coastal infrastructure but also serve as critical benchmarks for validating forecasting systems and enhancing climate projections.

Despite significant advancements in computational capabilities and numerical modeling techniques, the reliability of hindcasted wave fields remains constrained by uncertainties inherent to model inputs, namely forcing fields (Teixeira et al., 1995; Campos et al., 2022) and model parameters (Alday et al., 2022), by structural assumptions, namely the modeling and parametrization choices that specify the functional form of the system (Du et al., 2019), and by observational data (Dodet et al., 2020; Bitner-Gregersen et al., 2022). Structural and parameter uncertainties in wave models are inherently interconnected (Alonso and Solari, 2021). Hindcast wave databases are typically built using third-generation wave models that solve the wave action balance equation, allowing realistic reconstruction of historical sea states. These models simulate key physical processes such as wind input, wave dissipation, and nonlinear interactions through various parameterizations embedded in source and sink terms included in the wave action balance equation.

Parameterization choices define the model's structure and critically influence its ability to represent diverse sea states and adapt to environmental variability. Differences in parameterization schemes can significantly affect wave characteristics and model fidelity (Bi et al., 2015; Kalourazi et al., 2021), highlighting the need for rigorous and context-specific selection.

Once a model structure is selected, parameter calibration becomes essential to accurately simulate and represent physical processes. This step involves tuning uncertain, physically-based parameters to align model outputs with observed data. In wave modeling, where empirical formulations and non-measurable parameters are common, calibration significantly enhances model fidelity and predictive performance (Majidi et al., 2023). It reduces inherent uncertainties and strengthens the model's reliability for both operational forecasting and scientific analysis. As highlighted by Oreskes et al. (1994), calibration is key to achieve "empirical adequacy", the degree to which a model replicates observed phenomena. Traditionally, calibration relies on manual, heuristic trial-and-error, where parameters are iteratively adjusted and evaluated after each simulation. While straightforward, this method is labor-intensive, subjective, and often lacks a unique solution due to equifinality, where different parameter sets yield similar results (Simmons et al., 2017). As an alternative, deterministic optimization methods, such as those used by Dubarbier et al. (2015), offer a more systematic and reproducible calibration process. However, they still fall short in fully addressing uncertainties in both observations and model structure (Alonso and Solari, 2021).

Stochastic approaches provide robust alternatives to manual, deterministic calibration methods for parameter estimation and uncertainty quantification. The Generalized Likelihood Uncertainty Estimation (GLUE) algorithm exemplifies a pragmatic, brute-force strategy, employing Monte Carlo sampling to evaluate parameter sets against user-defined criteria without requiring a formal likelihood function (Simmons et al., 2017, 2019; Kroon et al., 2020). This makes GLUE suitable for models with poorly characterized error structures. However, its reliance on uniform priors and random sampling limits efficiency and statistical rigor in high-dimensional spaces (Vrugt and Beven, 2018).

Bayesian inference offers a more formal framework by integrating prior knowledge with observational data via a likelihood function, yielding posterior distributions that quantify parameter uncertainty. When implemented through Markov Chain Monte Carlo (MCMC) methods, Bayesian calibration accommodates nonlinearities and multimodal distributions (Alonso and Solari, 2021). Due to computational constraints, Bayesian methods are typically applied to approximated models, including physically-based models with coarser spatial or temporal resolutions (Alonso and Solari, 2021) and surrogate models that emulate complex system behavior (Ruessink, 2006; Solari and Alonso, 2022), with prior and likelihood assumptions guiding Bayesian processes such as data assimilation (Deltires, 2009; Goeury et al., 2024).

Recent advances in artificial intelligence have positioned Bayesian Optimization as a powerful and efficient solution for model calibration, particularly in the context of complex and computationally expensive models. As machine learning architectures grow in complexity, hyperparameter tuning becomes increasingly demanding, prompting the development of scalable, automated optimization frameworks and advanced search algorithms capable of navigating high-dimensional parameter spaces (Akiba et al., 2019).

Bayesian Optimization (BO) addresses these challenges by framing calibration as a global optimization problem. Through adaptive sampling, it efficiently explores non-convex objective functions without relying on gradient information, making it especially suitable for black-box models. Moreover, its ability to scale to high-dimensional parameter spaces and adapt to heterogeneous data sources makes it especially well suited for environmental applications, which often involve complex physical processes and large computational costs (Mouris et al., 2023; Tanim et al., 2024; Mrozowska et al., 2025).

This work introduces a novel integration of the Tree-structured Parzen Estimator (TPE) (Bergstra et al., 2011), selected for its ability to handle both continuous and categorical variables and to scale effectively in irregular, high-dimensional spaces. Embedded within a unified framework, this approach enables joint optimization of numerical parameters and discrete model structures, supporting a fully automated and comprehensive calibration process. By leveraging AI-driven hyperparameter optimization, the proposed methodology represents a significant advancement in the design of efficient, flexible, and scalable calibration workflows.

The structure of this paper is as follows. Section 2 introduces the ANEMOC-3 hindcast wave numerical database and outlines the dataset employed in this study. Section 3 presents the governing equations used in the simulations, along with the relevant physical and numerical parameters. Section 4 describes the probabilistic framework adopted for BO, including the materials and methods applied. The results of the

simulations and optimization procedures are reported in Section 5, followed by a critical discussion in Section 6. Finally, Section 7 summarizes the main contributions of the work and offers perspectives for future research.

2 Case Study

2.1 ANEMOC-3 hindcast wave numerical database

The ANEMOC hindcast database (in French “Atlas Numérique d’Etats de Mer Océaniques et Côtiers”) is derived from numerical simulations with TOMAWAC spectral wave model (Benoit et al., 1996), from the openTELEMAC numerical platform (www.opentelemac.org), and provides sea state conditions across various geographic domains. Developed jointly by EDF R&D LNHE and Cerema (which stands for Centre for Studies and Expertise on Risks, the Environment, Mobility and Urban Planning) over 16 years ago, its primary focus is on the French coastal areas of the Atlantic Ocean, English Channel, and North Sea (Benoit et al., 2008). This study presents the ANEMOC-3 version, covering the time period 1979–2024 and built using three computational nested meshes (Figure 1). The oceanic mesh, comprising 12,340 nodes and 23,542 elements (Figure 1a), covers nearly the whole the Atlantic ocean from 60°S to 80°N with an unstructured mesh of variable resolution, with the finest near the european waters with 0.15° resolution. The latter supplies directional variance spectra at open boundaries to the coastal mesh which has 56,375 nodes and 108,551 elements (Figure 1c), covering the French coastline beyond the 100 m isobath with a mesh resolution up to 0.01°, e.g roughly 1 km.

Bathymetry was interpolated from the 800 m resolution LEGOS “Europe” dataset at mean sea level, with GEBCO (General Bathymetric Chart of Oceans) data (30 arc-second resolution) supplementing uncovered regions of the oceanic mesh. Atmospheric forcing is taken from the NOAA reanalysis CFSR ($0.313^\circ \times 0.312^\circ$) and CFSv2 ($0.205^\circ \times 0.204^\circ$) data for 1979-2010 and 2011-2024 time periods respectively

To incorporate tidal effects on wave propagation in ANEMOC-3’s coastal domain, a coupled modeling approach was implemented by Raoult et al. (2018), combining the TELEMAC-2D hydrodynamic model (Hervouet, 2007) with the TOMAWAC spectral wave model, both components of the openTELEMAC hydro-informatic system. TELEMAC-2D first operates on a mesh covering the North Sea and french coastal waters using harmonic constituents imposed at open boundaries (Figure 1b). These are derived from the regional North-East Atlantic (NEA) tidal atlas, which provides amplitudes and phases for tidal elevation and horizontal current components (Pairaud et al., 2008, 2010). This first level domain gives the tidal water levels and currents to the coastal mesh, where TELEMAC-2D also operates by computing tidal water levels and currents every 15 minutes. The resulting tidal fields are taken into account by TOMAWAC to consider tidal modulation of wave dynamics on the coastal domain.

TOMAWAC solves the wave action balance equation (Benoit et al., 1996). For the ANEMOC-3 numerical wave database, it employs a spectral discretization of 32 frequency components ranging from 0.0345 Hz to 0.6622 Hz (corresponding to wave periods between 1.51 s and 29 s), and 36 directional bins with an angular resolution of 10°. The model uses a time step of 5 min in the oceanic domain and 30 s in the coastal domain to ensure temporal resolution appropriate to each scale. The wave model explicitly accounts for the fundamental physical processes governing wave dynamics, including wind-wave generation, wave breaking dissipation, nonlinear wave interactions, and bottom friction dissipation. These processes are represented using the BAJ formulation (Bidlot et al., 2007), which integrates Janssen’s wind input parameterization (Janssen, 1991), whitecapping dissipation following Komen et al. (1984), nonlinear quadruplet interactions computed via the Discrete Interaction Approximation (DIA) method (Hasselmann and Hasselmann, 1985), and bottom friction modeled according to the parameterization proposed by Bouws and Komen (1983). In the coastal domain, additional mechanisms are included to account for depth-induced wave breaking and strong opposing current-induced dissipation. The detailed parameterization of these processes are presented in the following sections. Further information on the configuration of ANEMOC-3 is available in Teles et al. (2022).

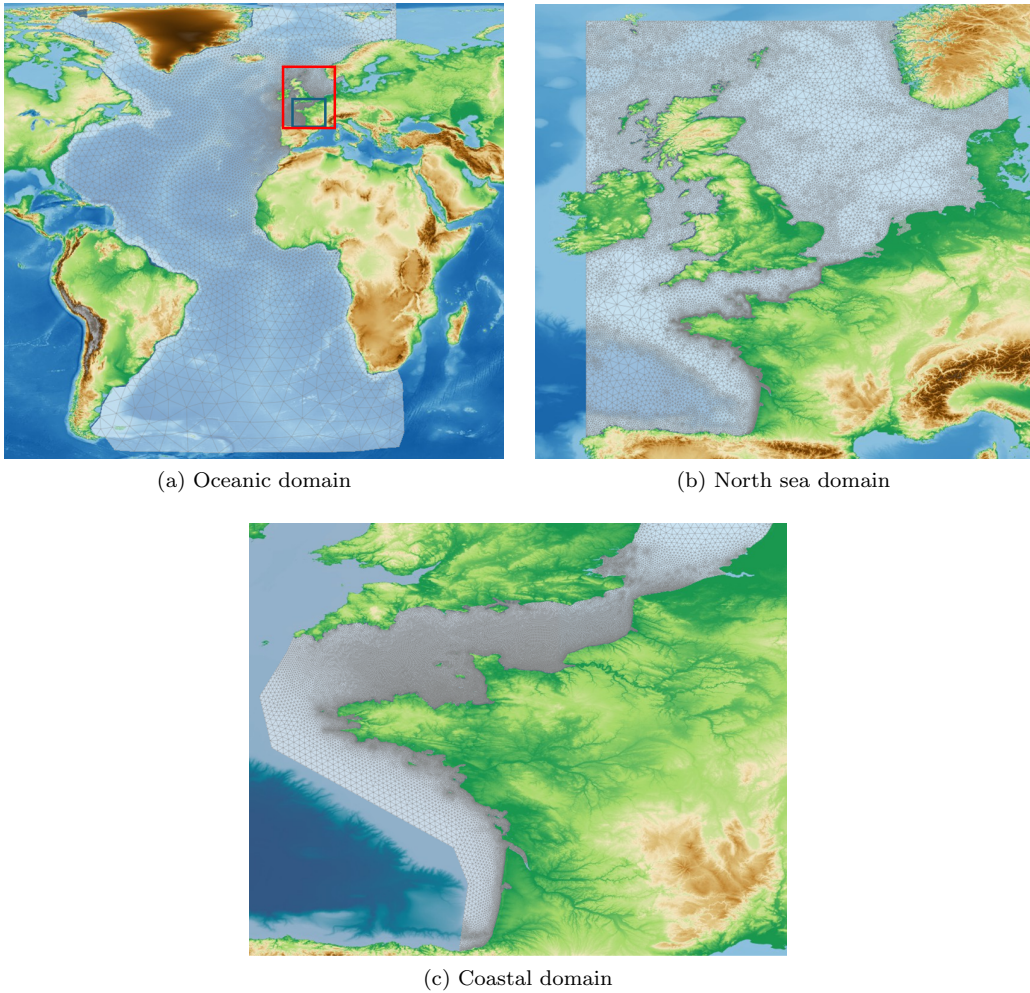


Figure 1: ANEMOC-3: Oceanic, North Sea and Coastal domains (1979–2024).

2.2 Measurement data

Wave measurements used for model calibration and validation are sourced from both offshore (deep water) and coastal (intermediate water) buoy stations, spanning water depths from approximately 20 meters to 4300 meters (Figure 2). These data are provided by the French CANDHIS network (Centre d'Archivage National des données de Houles In-Situ, <https://candhis.cerema.fr>), managed by Cerema, and the UK Met Office (UKMO) through the WaveNet system operated by Cefas (<https://wavenet.cefas.co.uk>). The CANDHIS network comprises over 40 waverider buoys deployed across mainland France and overseas territories, offering high-resolution wave data in real time and delayed mode. Similarly, the UKMO WaveNet network includes strategically placed buoys around the UK coastline, delivering continuous wave observations for operational forecasting and coastal monitoring.

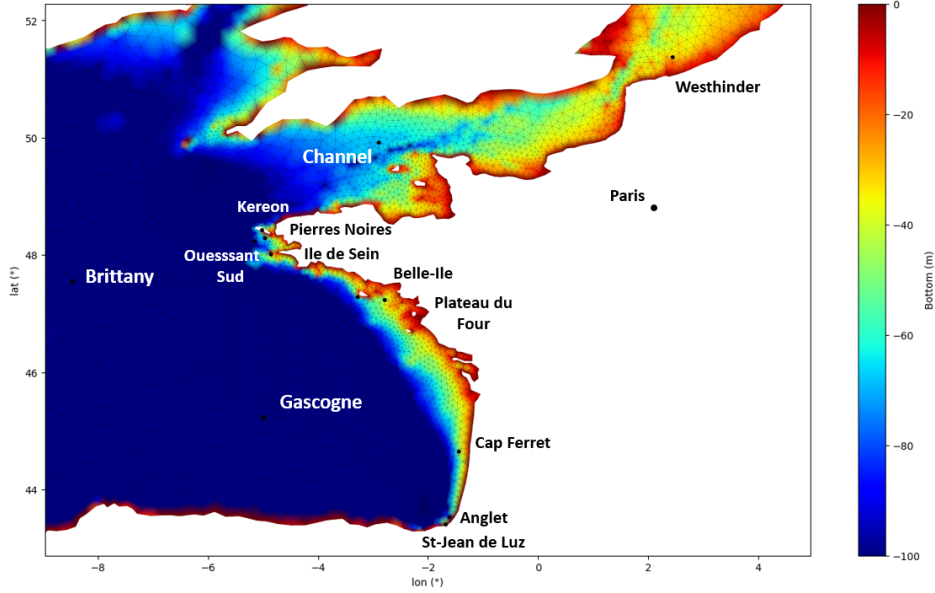


Figure 2: Bottom elevation and location of buoys considered over the ANEMOC-3 oceanic model.

Spectral significant wave height (H_{m0}) is recorded every 30 minutes by CANDHIS buoys and every 60 minutes by UKMO buoys. For calibration purposes, particular focus is placed on the period of February 2014, which was marked by a series of intense storm events that impacted severely the atlantic french coast. As illustrated in Figure 3, the Brittany buoy (UKMO 62163), positioned offshore in the Atlantic Ocean, recorded four storms during this period, each with maximum values of significant wave heights (H_{m0}) exceeding 10 meters. Notably, during the first half of February 2014, H_{m0} remained consistently above 4 meters, with maximum values reaching up to 13–14 meters. This high-energy period provides a robust dataset for calibrating wave model performance under such extreme conditions.

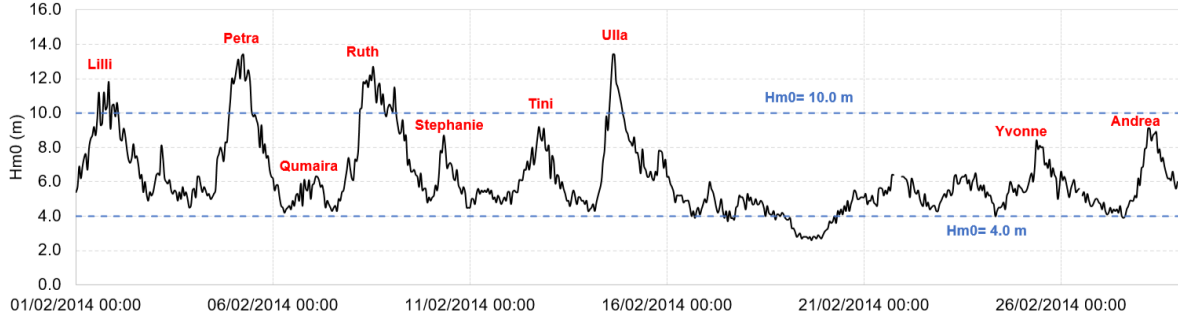


Figure 3: Significant wave height evolution during the months of January and February 2014 measured at Brittany buoy (UKMO 62163) with storm names highlighted in red.

3 Governing equations

3.1 The wave action conservation equation

TOMAWAC numerically solves the wave action balance equation, including energy source and dissipation mechanisms through semi-empirical parameterizations. The principal variable used to characterize the sea state is the directional wave energy spectrum, hereafter denoted by E . This spectrum provides a comprehensive representation of the distribution of wave energy across frequencies and directions. From the directional spectrum E , the wave action density N can be derived using the following relationship:

$$N = E/\rho g \sigma = F/\sigma \quad (1)$$

where σ denotes the relative or intrinsic angular frequency, i.e. the angular frequency being observed in a coordinate system moving at the velocity of current, ρ the water density, g the gravitational acceleration and F the directional variance spectrum.

TOMAWAC solves the following action flux conservation or balance equation:

$$\frac{\partial N}{\partial t} + \frac{\partial(\dot{x}N)}{\partial x} + \frac{\partial(\dot{y}N)}{\partial y} + \frac{\partial(\dot{k}_x N)}{\partial k_x} + \frac{\partial(\dot{k}_y N)}{\partial k_y} = Q(k_x, k_y, x, y, t) \quad (2)$$

where x and y are the horizontal Cartesian coordinates, t is time, k_x and k_y the wave number for directional spectrum discretization along x and y coordinates respectively and $Q(k_x, k_y, x, y, t)$ are the source, transfer and sink terms. The dot notation (e.g., \dot{x} , \dot{k}_x) denotes the rates of change of the respective variables, reflecting wave propagation in physical and spectral space.

The source and sink terms that compose $Q(k_x, k_y, x, y, t)$ in the right-hand members of Eq. 2 gather the contributions from the physical processes listed in Eq. 3.

$$Q = \underbrace{Q_{\text{in}}}_{\substack{\text{Wind} \\ \text{input}}} + \underbrace{\underbrace{Q_{\text{ds}}}_{\substack{\text{Whitecapping} \\ \text{friction}}} + \underbrace{Q_{\text{bf}}}_{\substack{\text{Bottom} \\ \text{friction}}} + \underbrace{Q_{\text{br}}}_{\substack{\text{Breaking} \\ \text{friction}}} + \underbrace{Q_{\text{ds,cur}}}_{\substack{\text{Strong} \\ \text{current}}} + \underbrace{Q_{\text{veg}}}_{\substack{\text{Vegetation}}} + \underbrace{Q_{\text{porous}}}_{\substack{\text{Porous} \\ \text{medium}}}}_{\text{Dissipation}} + \underbrace{Q_{\text{nl}} + Q_{\text{tr}}}_{\substack{\text{Quadruplets} \\ \text{Triads}}}_{\text{Transfers within the spectrum}} \quad (3)$$

In this study, particular attention is given to dissipation mechanisms that are especially relevant in the coastal domain of ANEMOC-3, characterized by limited-depth environments. These include the bottom friction dissipation term (Q_{bf}), the depth-induced breaking dissipation term (Q_{br}), and the wave dissipation associated with strong opposing currents ($Q_{\text{ds,cur}}$). These processes are critical in governing wave energy attenuation and transformation in shallow water regions, where their influence on the resulting sea state becomes increasingly significant. A detailed description of each term is provided in the following sections.

3.1.1 Bottom friction-induced dissipation

Bottom friction-induced wave energy dissipation is modeled using an empirical formulation that captures the combined effects of wave-seabed interactions, including percolation and frictional resistance. In this study, a linearized version of the original expression proposed by Hasselmann et al. (1973) is employed, which simplifies the representation while retaining the essential physical characteristics of the dissipation process. The adopted formulation is expressed as follows:

$$Q_{\text{bf}} = -\Gamma \frac{2k}{g \sinh(2kh)} F \quad (4)$$

where Γ is a constant dissipation coefficient, h is the local water depth, and $k = \sqrt{k_x^2 + k_y^2}$ is the wave number magnitude.

The parameter Γ , typically set to $0.038 \text{ m}^2 \cdot \text{s}^{-3}$, governs the intensity of wave energy dissipation resulting from wave-seabed interactions. This value is consistent with estimates derived from the JONSWAP experiment (Hasselmann et al., 1973), and is widely adopted in spectral wave modeling as a standard baseline for representing bottom friction across a variety of coastal and oceanic environments. In practical applications, Γ serves as a tunable calibration coefficient, allowing for adjustments to account for site-specific seabed characteristics.

3.1.2 Depth-induced breaking dissipation

To represent depth induced wave energy dissipation, parametric spectral models that estimate total energy loss by combining a breaking probability with a rate of energy dissipation can be adopted. Originally developed for random wave fields, these models are based on the formulations proposed by Battjes and Janssen (1978a) and Thornton and Guza (1983), and are described in the following sections. Despite differences in the model implementation, all approaches share a common conceptual foundation, drawing an analogy with hydraulic jumps. In the directional spectrum formulation, it is assumed that wave breaking reduces the total energy without modifying its distribution across frequencies and directions.

The characteristic frequency f_c , employed in both formulations, is chosen by the modeler. In this study, it corresponds either to the spectral peak frequency, or to representative mean frequencies such as $f_{01} = \frac{m_1}{m_0}$, where m_n denotes the n -th order spectral moment.

- Battjes and Janssen's model

The dissipation term introduced by Battjes and Janssen (1978a) assumes that all breaking waves reach a characteristic height H_m , which is approximately proportional to the local water depth h . Based on this assumption, the breaking-induced dissipation source term Q_{br} is formulated to preserve the spectral shape of the wave energy while accounting for the total energy loss due to breaking. The dissipation is distributed proportionally across the spectrum, and the expression is given by:

$$Q_{\text{br}} = -\frac{\alpha Q_b f_c H_m^2}{4} \cdot \frac{F}{m_0} \quad (5)$$

where, α is a dimensionless coefficient of order 1, Q_b is the fraction of breaking waves, f_c is a characteristic wave frequency, H_m is the maximum wave height associated with breaking, F is the directional variance spectrum, m_0 is the zeroth-order spectral moment (total wave energy).

The breaking fraction Q_b is computed from the Battjes and Janssen model as the solution of the implicit equation:

$$\frac{1 - Q_b}{\ln Q_b} = -\frac{H_{m0}^2}{2H_m^2}$$

where H_{m0} is the root-mean-square wave height of the incident sea state.

The model assumes that the cumulative distribution function of wave heights is given by a Rayleigh distribution, which is abruptly truncated at $H = H_m$ to represent the physical limit imposed by wave breaking. The characteristic wave height H_m used in the breaking-induced dissipation model can be estimated either through a linear relation $H_m = \gamma_2 h$, or using a formulation derived from Miche's criterion:

$$H_m = \frac{\gamma_1}{k_c} \tanh \left(\frac{\gamma_2 k_c h}{\gamma_1} \right)$$

where k_c is the magnitude of the wave number vector associated with the characteristic frequency f_c , obtained from the linear dispersion relation. The empirical coefficients γ_1 and γ_2 are calibration parameters that control the limiting steepness and depth dependence of breaking.

- Thornton and Guza's model

The wave breaking model proposed by [Thornton and Guza \(1983\)](#) describes energy dissipation using two statistical formulations for the distribution of breaking wave heights. The first, referred to as the uniform breaking formulation in Eq. 6, assumes that all wave heights contribute equally to energy dissipation. The second, known as the weighted breaking formulation (also in Eq. 6), gives greater weight to waves with larger heights, reflecting observational evidence that breaking predominantly affects higher waves. This refinement yields a more realistic representation of wave breaking in natural sea states. The corresponding energy sink term Q_{br} is expressed according to the selected wave height distribution.

$$Q_{br} = \begin{cases} \text{Uniform breaking : } -48\sqrt{\pi}b^3f_c \frac{(2m_0)^{5/2}}{H_m^4h} F \\ \text{Weighted breaking: } -12\sqrt{\pi}b^3f_c \frac{(2m_0)^{3/2}}{H_m^2h} \left[1 - \left(1 + \frac{8m_0}{H_m^2} \right)^{-5/2} \right] F \end{cases} \quad (6)$$

Here, f_c denotes the characteristic wave frequency. The parameter b , typically ranging from 0.8 to 1.5, serves as a calibration coefficient. The maximum wave height compatible with the local water depth, H_m , is defined as $H_m = \gamma h$, where γ is an empirical breaking parameter.

3.1.3 Wave blocking effects

Wave blocking occurs when surface waves propagate against a strong opposing current and the current velocity approaches the wave group velocity, leading to a reduction or cessation of wave energy transmission. Accurate representation of this process is critical for realistic wave modeling in regions with strong ambient flows. This study evaluates two common approaches for incorporating wave blocking in spectral wave models: equilibrium spectrum limitation, which constrains wave energy based on physical thresholds, and dissipative source terms, which simulate energy loss due to blocking.

- Equilibrium spectrum limitation

This method applies an upper bound to the wave energy spectrum based on a Phillips-type formulation ([Phillips, 1977](#)). When the spectral energy exceeds a threshold defined by a f^{-5} decay law, the spectrum is rescaled to maintain consistency with the theoretical maximum energy, given by Phillips's constant ($\alpha_p = 0.0081$):

$$\text{If } E(f) > E_{\max} = \frac{\alpha_p g^2}{(2\pi)^4 f^5}, \quad \text{then } F = \frac{E_{\max}}{E} F \quad (7)$$

This approach ensures that the high-frequency tail of the spectrum remains physically realistic under strong opposing currents.

- Dissipative source terms for wave-current interaction ($Q_{ds,cur}$)

Wave blocking is represented through an enhanced dissipation mechanism proposed by [van der Westhuyzen \(2012\)](#), which increases whitecapping dissipation in regions where wave steepness is amplified by opposing currents. The additional source term is defined as:

$$Q_{ds,cur} = -C_{ds,cur} \max \left(\frac{\dot{f}_r}{f}, 0 \right) \left(\frac{B(k)}{B_r} \right)^{p_0/2} F \quad (8)$$

Here, \dot{f}_r is the intrinsic frequency shift due to the current. The saturation parameter is given by $B(k) = C_g k^3 \frac{E(f)}{2\pi}$, with C_g denoting the group velocity. The exponent p_0 is defined as:

$$p_0 = 3 + \tanh \left[w \left(\frac{u_*}{C} - 0.1 \right) \right] \quad (9)$$

where $w = 25$ as used in [van der Westhuyzen et al. \(2007\)](#), u_* is the friction velocity, and C is the phase speed. The parameters B_r and $C_{ds,cur}$ are model constants representing the saturation threshold and dissipation scaling, respectively.

3.2 Model parameters

In summary, the simulation of wave energy dissipation within the ANEMOC-3 coastal domain relies on a set of parameterizations that describe key physical processes, including bottom friction, depth-induced wave breaking, and wave blocking caused by opposing currents. These processes are governed by a combination of continuous and discrete parameters, and their accurate representation under site-specific conditions requires careful calibration. This study concentrates on three principal mechanisms. Bottom friction is characterized by the coefficient Γ , which quantifies the energy lost through interaction with the seabed. Depth-induced wave breaking is modeled using a characteristic frequency, chosen either as the spectral peak or a representative mean frequency, and is described through two alternative formulations. The first is the model proposed by [Battjes and Janssen \(1978a\)](#), which incorporates the parameters α , γ_2 , and γ_1 , particularly when Miche's criterion is applied to estimate the maximum wave height H_m . The second is the formulation by [Thornton and Guza \(1983\)](#), which primarily depends on the parameters γ and b . Wave blocking due to opposing currents is addressed using either the equilibrium spectrum limitation or a dissipative source term, the latter involving parameters such as the dissipation coefficient $C_{ds,cur}$ and the reference blocking parameter B_r . The ranges of variation for these parameters are detailed in the following sections.

3.2.1 Bottom friction-induced dissipation

As already mentioned, bottom friction plays a critical role in wave energy dissipation, particularly in shallow coastal and shelf regions. Empirical studies have provided a range of values for the bottom friction dissipation coefficient, Γ , depending on seabed characteristics and wave conditions. In the JONSWAP experiment, [Hasselmann et al. \(1973\)](#) proposed a value of $\Gamma = 0.038 \text{ m}^2 \text{ s}^{-3}$ for swell dissipation over sandy bottoms. This was later revised by [Bouws and Komen \(1983\)](#), who suggested $\Gamma = 0.067 \text{ m}^2 \text{ s}^{-3}$ for fully developed wind seas. Subsequent research has broadened the applicable range to values between 0.003 and 0.15 ([Padilla-Hernández and Monbaliu, 2001](#); [Cialone and Smith, 2007](#); [Bastidas et al., 2016](#)). These findings collectively support the adoption, in the current study, of a generalized range of 0.01 to 0.1 for Γ in wave models, providing a balance between physical realism and model flexibility across diverse seabed conditions.

3.2.2 Bathymetry breaking-induced dissipation

- Battjes and Janssen's model

In the TOMAWAC implementation of the [Battjes and Janssen \(1978b\)](#) depth-induced breaking formulation, three empirical coefficients control the dissipation rate: γ_1 , γ_2 , and α . The model defaults are $\gamma_1 = 0.88$, $\gamma_2 = 0.80$, and $\alpha = 1.0$. Physically, γ_2 sets the maximum individual wave height relative to local depth, defining the onset of depth-limited breaking; γ_1 adjusts the shape of the breaking probability function and the effective breaker height, influencing the fraction of waves assumed to break; and α is a linear scaling factor on the dissipation term, directly controlling the magnitude of energy loss once breaking occurs. Because the [Battjes and Janssen \(1978b\)](#) formulation relies on simplified assumptions, such as Rayleigh statistics for wave heights and a hydraulic jump analogy (i.e., treating wave breaking as similar to a sudden water level rise for estimating energy dissipation), the associated coefficients do not have universal values and must be calibrated to local conditions.

Field and laboratory calibrations consistently report breaker indices deviating from the original value of $\gamma_2 = 0.80$, with observed values ranging between approximately 0.4 and 1.5 depending on bathymetry, slope, and spectral shape ([Battjes and Stive, 1985](#); [Kraus and Kaminsky, 1994](#); [Apotsos et al., 2008](#); [Carini et al., 2021](#)). Similarly, α has been calibrated in the literature over a range of approximately 0.2 to 1.2, and occasionally higher when compensating for other source-term settings ([Rattanapitikon and Karunchintadit, 2002](#); [Damlamian and Kruger, 2013](#)). Based on these findings, conservative calibration envelopes of $\gamma_1 \in [0.50, 1.20]$, $\gamma_2 \in [0.50, 1.20]$, and $\alpha \in [0.50, 1.50]$ are considered for this study. These ranges bracket theoretical benchmarks, model defaults, and the spread of empirical fits, while ensuring that site-specific optimal values can be identified through the calibration process.

- Thornton and Guza's model

The depth-induced wave breaking formulation developed by Thornton and Guza (1983) relies on two empirical parameters: γ , which modulates the spectral distribution of wave energy dissipation, and b , which scales its overall intensity. In TOMAWAC, the default parameter values are set to $\gamma = 0.42$ and $b = 1.0$; nevertheless, the model documentation highlights the critical need for site-specific calibration in order to accurately represent local wave transformation processes and energy dissipation dynamics. Allowing γ to vary within the interval $[0.2, 0.6]$ is consistent with both laboratory and field studies, where lower values tend to distribute dissipation more broadly across the wave spectrum, while higher values concentrate it on dominant wave components (Thornton and Guza, 1983; Apotsos et al., 2008; Gon, 2019). Similarly, the range $[0.5, 2.0]$ for b is supported by calibration exercises in coastal wave modeling, where b serves as a key tuning parameter to match observed wave decay and surf-zone setup (Thornton and Guza, 1983; van der Westhuyzen, 2010). These intervals offer sufficient flexibility to accommodate site-specific variability while maintaining physically realistic dissipation behavior.

3.2.3 Dissipative source terms for wave-current interaction

The formulation introduced by van der Westhuyzen (2012) enhances the representation of wave blocking effects induced by opposing currents by modifying the dissipation source term to incorporate the influence of current velocity on wave breaking. This refinement contributes to a more physically realistic modeling of wave-current interactions. The approach is governed by two key parameters: the saturation threshold B_r , which defines the onset of nonlinear wave breaking, and the dissipation scaling factor $C_{ds,cur}$, which adjusts the dissipation rate in response to current velocity. In this study, $C_{ds,cur}$ is varied within the range $[0.4, 0.9]$, in accordance with the original recommendations.

The parameter B_r plays a critical role in determining the initiation of wave breaking due to nonlinear saturation. Experimental findings by Banner et al. (2002) indicate that wave breaking typically begins when the saturation exceeds values between 0.001 and 0.002. This range was adopted and validated in the revised dissipation formulation by van der Westhuyzen et al. (2007), who demonstrated that lower saturation thresholds improve model performance across both deep and shallow water environments. These parameter ranges ensure consistency with observed wave-current interactions and support the physical realism of the dissipation behavior.

4 Bayesian optimization for Model Tuning

BO is a strategy for efficiently minimizing a black-box objective function, defined as $f : \mathcal{X} \rightarrow \mathbb{R}$, where \mathcal{X} denotes the space of possible parameter configurations. The goal is to identify the global minimizer $\boldsymbol{\theta}_{\text{opt}} \in \arg \min_{\boldsymbol{\theta} \in \mathcal{X}} f(\boldsymbol{\theta})$ without requiring explicit knowledge of the analytical form of f .

The optimization process relies on a set of n noisy observations $\mathcal{D}_n = \{(\boldsymbol{\theta}_i, e_i)\}_{i=1}^n$, where each observation is modeled as $e_i = f(\boldsymbol{\theta}_i) + \varepsilon$, with ε denoting stochastic noise. In a sequential decision-making framework, BO selects the next query point $\boldsymbol{\theta}_i$ by maximizing an acquisition function $\mathcal{L} : \mathcal{X} \rightarrow \mathbb{R}$, which strategically balances exploitation (sampling near previously promising points) and exploration (probing uncertain or under-sampled regions) to efficiently locate the global optimum. This sequential approach allows for efficient optimization with a minimal number of function evaluations, making it particularly suitable for hyperparameter tuning in machine learning and other domains where evaluations are computationally intensive. A widely used acquisition function in BO is the *Expected Improvement* (Jones et al., 1998), which quantifies the expected gain over the current best observation e^* such as:

$$\mathcal{L}(\boldsymbol{\theta}) = \int_{-\infty}^{e^*} (e^* - e) p(e|\boldsymbol{\theta}, \mathcal{D}_n) de \quad (10)$$

In this expression, the term $p(e|\boldsymbol{\theta}, \mathcal{D}_n)$ reflects the posterior belief about the function $f(\boldsymbol{\theta})$ given the data set \mathcal{D}_n . Estimating this probability has been widely studied, with various methods proposed in the literature. Gaussian Processes (GPs) are widely used surrogate models in BO due to their analytically tractable posterior distributions (Song et al., 2022). In this work, the Tree-structured Parzen Estimator (TPE) (Bergstra et al., 2011) is adopted for BO due to its practical advantages over Gaussian Processes (GPs). TPE demonstrates superior *scalability* (Bergstra et al., 2011), avoiding the $\mathcal{O}(n^3)$ complexity of

GP inference caused by covariance matrix inversion; enhanced *flexibility*, by natively supporting categorical and conditional hyperparameters through its tree-structured search space (Watanabe, 2023); and greater *efficiency* (Ozaki et al., 2022), leveraging non-parametric density estimation to capture multi-modal, non-Gaussian distributions and enable parallel, asynchronous evaluations.

4.1 Tree-structured Parzen Estimator

The Tree-structured Parzen Estimator (TPE) framework models parameter spaces using a tree-based structure, enabling the representation of conditional and hierarchical dependencies among the different tuning variables. Unlike traditional Bayesian optimization approaches that directly model the posterior $p(e|\boldsymbol{\theta}, \mathcal{D}_n)$, TPE estimates the inverse conditional density $p(\boldsymbol{\theta}|e, \mathcal{D}_n)$ and applies Bayes' theorem to recover the posterior. This inversion facilitates flexible, non-parametric modeling of complex configuration spaces. The conditional density $p(\boldsymbol{\theta}|e, \mathcal{D}_n)$ is defined piecewise based on a threshold e^* , typically chosen as a quantile $q \in (0, 1)$ of the observed objective values, such that $P(e < e^*) = q$. The formulation is given by:

$$p(\boldsymbol{\theta}|e, \mathcal{D}_n) = \begin{cases} p(\boldsymbol{\theta}|\mathcal{D}_n^l) = l(\boldsymbol{\theta}) & \text{if } e \leq e^* \\ p(\boldsymbol{\theta}|\mathcal{D}_n^g) = g(\boldsymbol{\theta}) & \text{if } e > e^*; \end{cases} \quad (11)$$

where, $l(\boldsymbol{\theta})$ denotes the density estimated from the subset of observations $\{\boldsymbol{\theta}_{(i)}\}$ for which the corresponding objective function $f(\boldsymbol{\theta}_{(i)})$ is less than the threshold e^* , while $g(\boldsymbol{\theta})$ is the density estimated from the remaining observations.

As demonstrated by Bergstra et al. (2011), this formulation allows the expected improvement acquisition function (Eq. 10) to be expressed as:

$$\mathcal{L}(\boldsymbol{\theta}) = \int_{-\infty}^{e^*} (e^* - e) \frac{p(\boldsymbol{\theta}|e, \mathcal{D}_n) p(e|\mathcal{D}_n)}{p(\boldsymbol{\theta}|\mathcal{D}_n)} de \propto \left(q + (1 - q) \frac{g(\boldsymbol{\theta})}{l(\boldsymbol{\theta})} \right)^{-1} \quad (12)$$

Thus, maximizing expected improvement corresponds to maximizing the density ratio $\frac{l(\boldsymbol{\theta})}{g(\boldsymbol{\theta})}$, favoring configurations with higher expected performance. The models $l(\boldsymbol{\theta})$ and $g(\boldsymbol{\theta})$ are constructed using kernel density estimation, capturing both discrete and continuous hyperparameters within a hierarchical framework. For the reader seeking further insight, the description of the algorithm components and their roles are described in Watanabe (2023). In the present work, the methodology described here before is performed based on an open-source library for hyperparameter optimization framework to automate hyperparameter search named “Optuna” (Akiba et al., 2019).

4.2 Practical strategies for physical link implementation

As presented in Section 3, the wave dynamics model employs empirical parameterizations to represent essential physical processes, including bottom friction, depth-induced wave breaking, and wave blocking due to opposing currents, which are the focus of this study. The control vector $\boldsymbol{\theta}$, introduced in Eq. 10, consists of the parameters described in Subsection 3.2. Since TOMAWAC (thereafter denoted M) operates on a spatially and temporally discrete framework, each realization $\boldsymbol{\theta}_j$ produces a model output Y that corresponds to buoy observations (see Subsection 2.2). For each point of interest \mathbf{x}_p , representing buoy-equivalent locations, the output consists of significant wave height values at discrete time steps $t \in [1, \dots, T]$, expressed as $Y = (Y_1, \dots, Y_T)$, where $Y_i = Y(\mathbf{x}_p, t_i) = M(\boldsymbol{\theta}_j; (\mathbf{x}_p, t_i))$. Reliable wave prediction across coastal environments requires that the numerical model closely aligns with historical observations of significant wave height. This alignment is achieved through a calibration process that minimizes discrepancies between model outputs and measurements at observation stations, by optimizing the following error metric:

$$f(\boldsymbol{\theta}) = \frac{1}{2} \left(\mathbf{Y}^{obs} - \mathcal{H}(M(\boldsymbol{\theta})) \right)^T \mathcal{W}^{-1} \left(\mathbf{Y}^{obs} - \mathcal{H}(M(\boldsymbol{\theta})) \right) \quad (13)$$

where \mathcal{W} is a weighting matrix that adjusts the relative influence of each observation based on local depth, assigning greater weight to shallower buoy data to enhance sensitivity to depth-dependent wave behavior, \mathcal{H} is an operator that projects the numerical output onto the observation space and $\mathbf{Y}^{obs} \in \mathbb{R}^{N_{obs}}$ denotes the vector of observed significant wave heights at buoy locations.

At this stage, a critical question arises: which observations (\mathbf{Y}^{obs}) should be incorporated into the calibration process? This issue is examined in detail in the following section.

4.2.1 Selection of the calibration data subset

To investigate the spatial variability of model errors across buoy measurement sites, a Principal Component Analysis (PCA) was performed on the error fields. These errors were computed by comparing buoy observations with outputs from 1,000 ANEMOC-3 simulations generated using a Monte Carlo design of experiments. The model structure incorporated depth-induced breaking following Thornton and Guza (1983) and wave dissipation due to opposing currents as formulated by van der Westhuyzen (2012). PCA, a dimensionality reduction technique, transforms the original variables into a new set of orthogonal (uncorrelated) principal components that capture the maximum variance in the data.

The PCA correlation circle shown in Figure 4 illustrates the correlation between model errors at the buoy locations, projected onto the first two principal components, which together explain more than 99% of the total variance.

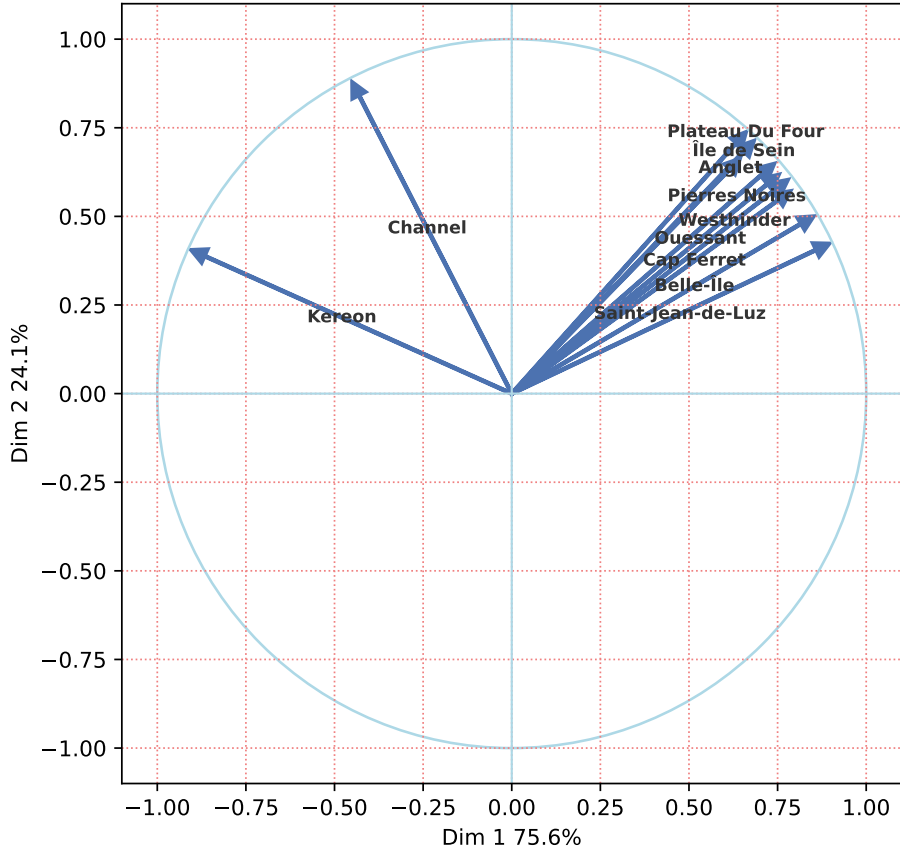


Figure 4: Correlation circle of the first two principal components of the PCA (explaining more than 99% of the total variance), illustrating model errors $f(\theta)$ across buoy measurement sites based on 1,000 Monte Carlo simulations using a model structure incorporating depth-induced breaking Thornton and Guza (1983) and wave dissipation due to opposing currents van der Westhuyzen (2012).

The correlation circle reveals distinct groupings among the buoy stations based on the similarity of their associated model errors. Two clearly separated clusters are observed: one comprising the *Kereon* and *Channel* buoys, and another including the remaining stations. To avoid introducing a trade-off between

these divergent groups during the calibration process, the *Kereon* and *Channel* buoys were excluded.

Among the remaining buoys, the angle between vectors in the correlation circle reflects the degree of correlation between their associated errors. Based on this criterion, three groups of correlated buoys can be identified: (i) *Plateau du Four*, *Île de Sein*, and *Anglet*; (ii) *Pierres Noires*, *Ouessant*, *Cap Ferret*, and *Westhinder*; and (iii) *Belle-Île* and *Saint-Jean-de-Luz*.

Although the error associated with the *Anglet* buoy is closely aligned with that of *Île de Sein* in the PCA space, its slightly weaker correlation and collinearity led to its exclusion in favor of the more representative *Île de Sein*.

To maintain balanced representation across groups and avoid overemphasizing any single cluster, the group composed of *Pierres Noires*, *Ouessant*, *Cap Ferret*, and *Westhinder* was reduced to two buoys. In this context, the two deeper buoys (*Ouessant* and *Westhinder*) were excluded to enhance sensitivity to depth-dependent wave behavior.

In summary, based on the correlation analysis, the buoy stations retained for model calibration in this study are: *Plateau du Four*, *Île de Sein*, *Pierres Noires*, *Cap Ferret*, *Belle-Île*, and *Saint-Jean-de-Luz*.

5 Results

BO is conducted here by coupling the TOMAWAC wave model with the open-source hyperparameter optimization framework “Optuna” (Akiba et al., 2019), within a Python environment via the TelApy component of the openTELEMAC system (Goeury et al., 2022). This methodology has been implemented using MPI technology on high-performance computing (HPC) resources, enabling parallel evaluation of distinct and independent samples. Such an approach ensures computational efficiency and meets the performance requirements of industrial applications.

As expressed in Eq. 13, the optimal estimation of the control vector θ is formulated as the minimization of an objective function that quantifies the discrepancy between model outputs and observational data. This optimization is performed using a Bayesian approach. The proposed methodology facilitates the simultaneous calibration of the model structure, defined by the choice of constitutive law, and the associated underlying parameter, within a unified optimization framework. Based on the correlation analysis, the observation vector \mathbf{Y}^{obs} corresponds to the spectral significant wave height (H_{mo}), recorded every 30 minutes by the CANDHIS network at the following buoy locations: *Plateau du Four*, *Île de Sein*, *Pierres Noires*, *Cap Ferret*, *Belle-Île*, and *Saint-Jean-de-Luz*, over the period from February 1 to March 1, 2014. In this study, the weighting matrix \mathcal{W} is specified as a diagonal matrix, with each diagonal entry representing the relative contribution of a buoy measurement. The weights are depth-dependent, favoring shallower buoys to enhance sensitivity to near-surface wave dynamics.

To assess the robustness of the calibration methodology, the optimization process was repeated six times using different initial guesses. The configuration yielding the lowest objective function value was selected as the optimal solution. Its consistent retrieval in three independent trials demonstrates the robustness of the optimal value. Figure 5 presents the evolution of the objective function across BO trials.

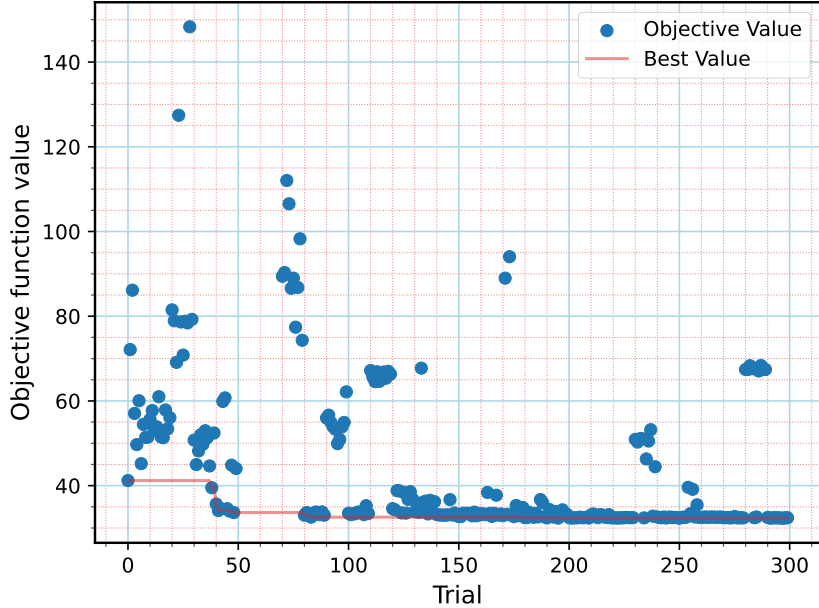


Figure 5: Evolution of the objective function value across trials during the optimization process. The plot shows both the objective value for each trial (•) and the best value (—) found up to that point, highlighting the convergence behavior of the optimization.

A clear downward trend in the best objective function value is observed, indicating a progressive enhancement in solution quality. After approximately 100 trials, the rate of improvement diminishes, suggesting that the optimization process is nearing convergence, with subsequent trials contributing incremental refinements to the solution. The optimal configuration for wave energy dissipation was obtained by employing the depth-induced breaking model of Thornton and Guza (1983), incorporating the weighted breaking formulation and adopting the characteristic frequency $f_c = f_{01}$. Wave energy dissipation due to wave-current interactions, particularly in the presence of opposing currents, was modeled using the formulation proposed by van der Westhuyzen (2012). The calibrated parameters for the Thornton and Guza model were determined to be $b = 1.129$ and $\gamma = 0.344$, while the Van der Westhuyzen formulation yielded optimal values of $C_{ds,cur} = 0.792$ and $B_r = 0.001$. Additionally, the parameter Γ , which governs wave energy dissipation due to wave-seabed interactions, was calibrated to $\Gamma = 0.053$.

Figure 6 presents the time series resulting from the calibration process conducted at the *Plateau du Four* buoy location over the simulation period. The model output generated using the optimized parameter set, denoted as $M(\boldsymbol{\theta}_{opt}; (\mathbf{x}_p, t))$ and referred to hereafter as the “re-analysis” or “optimized configuration”, is compared with the simulation obtained using the default parameter values, $M(\boldsymbol{\theta}_{dpv}; (\mathbf{x}_p, t))$, hereafter referred to as the “default parameter configuration” provided by the TOMAWAC solver.

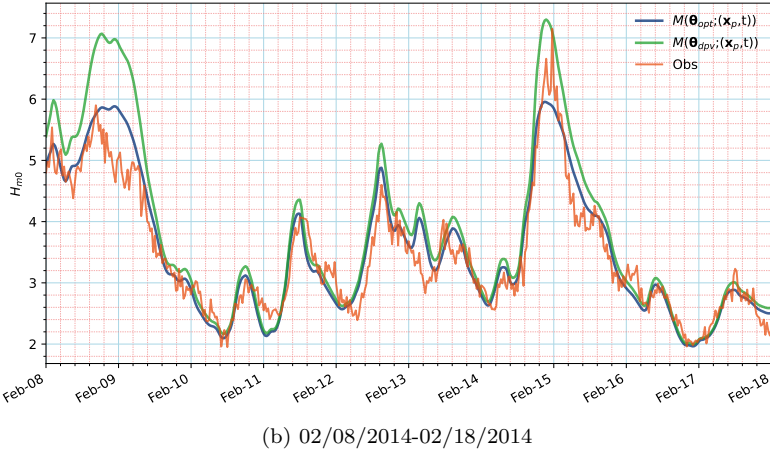
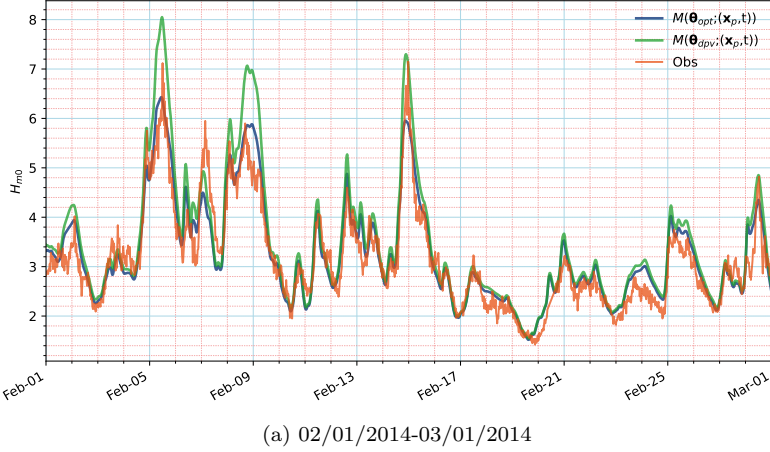
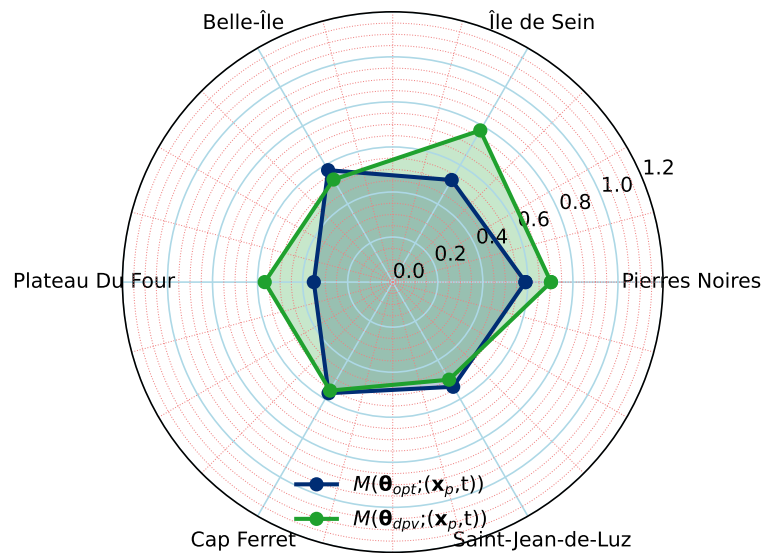
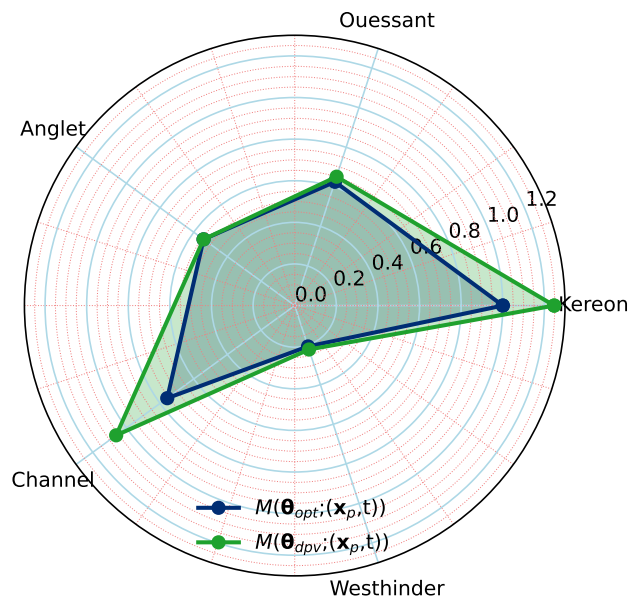


Figure 6: Comparison of the spectral significant wave height time evolution with and without calibration (respectively $\text{— } M(\boldsymbol{\theta}_{opt}; (\mathbf{x}_p, t))$ and $\text{— } M(\boldsymbol{\theta}_{dpv}; (\mathbf{x}_p, t))$) with respect to the buoy measurements at Plateau du Four ($\text{— } \text{Obs}$) during February 2014.

As anticipated, the spectral significant wave heights computed using the calibrated parameter configuration exhibit a markedly improved agreement with observational measurements compared to those obtained using the default parameter values. Figure 7 illustrates the Root Mean Square Error (RMSE) performance of the re-analysis methodology across two distinct sets of buoy locations along the French Atlantic coast. Specifically, Figure 7a focuses on the buoys employed during the calibration process, while Figure 7b presents results for independent validation buoys. In both cases, two model configurations are compared: the re-analysis configuration $M(\boldsymbol{\theta}_{opt}; (\mathbf{x}_p, t))$, which incorporates the calibrated parameters, and the reference default parameter configuration $M(\boldsymbol{\theta}_{dpv}; (\mathbf{x}_p, t))$, based on the default parameter set provided by the TOMAWAC solver.



(a) Calibrated buoys



(b) Validated buoys

Figure 7: Comparison of the root mean square error on spectral significant wave height evolution with and without calibration (respectively $\text{--- } M(\theta_{opt}; (x_p, t))$ and $\text{--- } M(\theta_{dpv}; (x_p, t))$) with respect to the buoy measurements during February 2014.

RMSE values reveal strong spatial variability, with the re-analysis model consistently outperforming the reference default parameter setup. Northern sites like *Pierres Noires* and *Île de Sein* show lower RMSE, indicating successful calibration. In contrast, southern buoys such as *Cap Ferret* and *Saint-Jean-de-Luz* display higher errors, likely due to complex local dynamics. *Cap Ferret*, for instance, is affected by energetic tides and shifting coastal morphology, which complicate wave modeling (Nahon et al., 2019). Notably, despite their proximity, *Belle-Île* and *Plateau du Four* exhibit contrasting performance. *Belle-Île* records higher RMSE values, even with calibration, likely due to its exposure to offshore swell and complex bathymetry. In contrast, *Plateau du Four* benefits from more stable conditions, resulting in better model performance when calibrated. These results emphasize that local physical characteristics, beyond geographic proximity, play a critical role in model accuracy and calibration effectiveness.

For the validation buoys, the re-analysis model also shows improved performance, particularly at *Kereon* and *Channel*. Although *Kereon* and *Ouessant* are geographically close to several calibration sites, they exhibit contrasting responses to the optimization process. *Ouessant*, being the deepest buoy and less influenced by the processes studied, shows limited improvement. In contrast, the positive results at *Channel* suggest a degree of spatial transferability of the calibration. However, at more distant locations such as *Anglet* and *Westhinder*, RMSE reductions are less significant, underscoring the limitations of extrapolating calibration effects over broader spatial scales. These findings highlight the importance of geographically distributed calibration and validation strategies to ensure robust and accurate coastal re-analysis.

Another key performance indicator is the scatter plot between observed versus modeled significant wave height results and the superposed the Quantile-Quantile (Q-Q) plot. A perfect agreement between the model and the observational data distributions is indicated when the Q-Q plot aligns precisely with the 45-degree diagonal line. Figure 8 compares modeled and observed significant wave heights (H_{m0}) at *Plateau du Four* buoy for the re-analysis and default setting configurations.

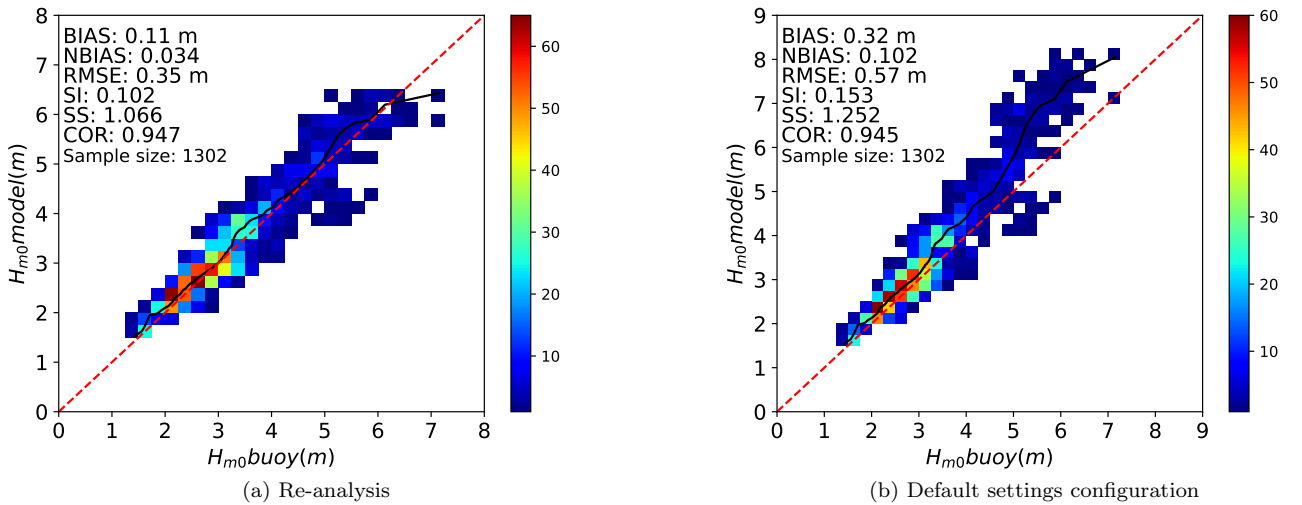


Figure 8: Scatter and Q-Q plots comparing modeled versus observed spectral significant wave heights (H_{m0}) at the *Plateau du Four* buoy for both the re-analysis and default parameter values configuration. Performance metrics include bias (BIAS, representing systematic error), normalized bias (NBIAS, indicating relative error), root mean square error (RMSE, quantifying overall error magnitude), scatter index (SI, measuring dispersion), skill score (SS, assessing predictive accuracy), and correlation coefficient (COR, reflecting linear association).

As shown in Figure 8, both models exhibit strong correlation with observations ($COR \approx 0.95$), but performance metrics reveal significant differences. The re-analysis configuration (Figure 8a) demonstrates lower bias (0.11 m), RMSE (0.35 m), and scatter index (0.102), with the Q-Q plot closely following the diagonal, particularly for mid-range values (2–5 m), indicating accurate distributional representation. Minor devia-

tions occur at higher wave heights (> 6 m), where the model tends to underestimate extremes. Conversely, the default parameter configuration (Figure 8b) shows higher bias (0.32 m), RMSE (0.57 m), and scatter index (0.153), with greater deviations at higher quantiles, suggesting overestimation and reduced reliability under extreme conditions. The wider spread of points in the default configuration confirms higher variability and less consistent performance compared to re-analysis.

6 Discussion

The results obtained in this study confirm the effectiveness of BO for calibrating wave model sink terms, particularly in the context of extreme sea state re-analysis. The integration of the TPE within a scalable optimization framework led to significant improvements in model fidelity, with reductions in RMSE and bias observed across multiple buoy locations. These outcomes demonstrate the potential of BO to enhance the representation of complex coastal wave dynamics, especially under high-energy conditions. Nevertheless, several methodological aspects warrant further investigation to improve model performance and generalizability.

One key limitation of the current implementation is the assumption of a spatially uniform bottom friction coefficient. This simplification may overlook important spatial heterogeneities in seabed composition, sediment type, and bathymetric features, which can significantly influence wave energy dissipation. Incorporating spatially variable bottom friction, informed by geophysical datasets or sedimentological maps, should allow the model to better capture local dissipation processes and improve accuracy in heterogeneous coastal environments.

Another area for improvement concerns enhancing the model's ability to represent fine-scale coastal dynamics. Although the calibration process has led to a significant reduction in discrepancies between model outputs and observations, persistent residual errors remain at specific buoy locations, such as *Cap Ferret* and *Belle-Île*. These mismatches suggest that local processes, potentially influenced by complex bathymetry, tidal interactions, and nearshore dynamics, are not adequately resolved. Addressing these limitations through increased spatial resolution of the computational mesh and, where appropriate, coupling with higher-resolution hydrodynamic models could substantially improve the representation of localized wave transformations, thereby enhancing calibration accuracy and overall predictive performance.

The current optimization strategy focuses on minimizing a single objective function based on significant wave height. While effective, this approach may not fully capture the trade-offs between different aspects of model performance. Extending the framework to a multi-objective optimization setting would enable simultaneous calibration across multiple metrics, such as mean wave behavior, extreme event representation, and spectral characteristics. This would provide a more balanced and comprehensive calibration strategy, particularly for applications involving risk assessment or operational forecasting. Furthermore, the calibration process could benefit from the analysis of additional spectral outputs. Parameters such as peak wave period, mean wave direction, and directional spreading offer valuable insights into the wave field structure and energy distribution. Incorporating these outputs into the optimization process would support a more holistic tuning of the model and improve its performance across a broader range of wave characteristics.

While BO efficiently identifies optimal parameter sets, it does not inherently provide a probabilistic characterization of uncertainty. A comprehensive understanding of parameter sensitivity and model robustness requires the integration of uncertainty quantification techniques. In this context, methods such as Markov Chain Monte Carlo (MCMC) sampling, particularly when combined with surrogate modeling to mitigate computational costs, offer a promising avenue for estimating posterior distributions of model parameters. This probabilistic insight would enable the assessment of confidence intervals associated with both model inputs and outputs, thereby enhancing the interpretability of calibration results. Such an approach is especially valuable in operational settings, where informed decision-making depends not only on model accuracy but also on a transparent evaluation of uncertainty.

Taken together, these avenues for refinement highlight the adaptability of the BO framework and its potential for broader application in modeling geophysical flows and waves. By addressing these methodological challenges, future work can further improve the accuracy, reliability, and utility of wave model calibration in coastal and oceanographic studies.

7 Conclusion

This study has demonstrated the benefits of using Bayesian Optimization (BO) as a robust and efficient framework for calibrating a set of sink terms of a spectral wave model, with a focus on the ANEMOC-3 hindcast wave database. By embedding the Tree-structured Parzen Estimator (TPE) into the calibration process, the methodology achieved significant improvements in model–observation agreement, particularly during extreme sea state events. The optimized configuration outperformed the default TOMAWAC setup across multiple metrics, including RMSE, bias and scatter index, while maintaining strong correlation with in-situ buoy measurements.

Beyond the specific case study, the proposed framework supports joint optimization of continuous parameters and discrete model structures, such as the selection of physical parameterizations. Its scalability and compatibility with the openTELEMAC system make it readily applicable to a wide range of geophysical modeling applications, including water quality, hydrodynamics, and morphodynamics. Moreover, the integration of multi-objective optimization and uncertainty quantification techniques offers promising avenues for future research. In summary, the adoption of AI-driven optimization strategies such as BO represents a significant advancement in the calibration of complex environmental models. This work lays the groundwork for more reliable, efficient, and adaptive modeling systems, ultimately contributing to improved ocean and coastal forecasting and hindcasting capabilities.

Acknowledgements

This work was carried out as part of EDF R&D’s MOISE-2 research project on river and coastal flood hazard assessment, whose support the authors gratefully acknowledge. The authors gratefully acknowledge contributions from the open-source community, especially that of the open source hyperparameter optimization framework to automate hyperparameter search library Optuna.

Declarations

Competing interests The authors have no competing interests to declare that are relevant to the content of this article.

References

- M. Accensi, G. F. M. Alday, C. Maisondieu, N. Raillard, D. Darbynian, C. Old, B. Sellar, O. Thilleul, Y. Perignon, G. Payne, L. O’boyle, L. Fernandez, F. Dias, R. Chumbinho, and G. Guitton. Resourcecode framework: A high-resolution wave parameter dataset for the european shelf and analysis toolbox. In *Proceedings of the 14th European Wave and Tidal Energy Conference*, pages 2182–1–2182–9, Plymouth, UK, 2021.
- T. Akiba, S. Sano, T. Yanase, T. Ohta, and M. Koyama. Optuna: A Next-generation Hyperparameter Optimization Framework, 2019. Preprint at <https://doi.org/10.48550/arXiv.1907.10902>.
- A. Akpinar, G. Besio, and B. Kamranzad. Editorial: Advances in sea state modeling and climate change impacts. *Front. Mar. Sci.*, Volume 10 - 2023, 2023. doi: 10.3389/fmars.2023.1151020.
- M. Alday and G. Lavidas. The echowave hindcast: A 30-years high resolution database for wave energy applications in north atlantic european waters. *Renew. Energy*, 236:121391, 2024. ISSN 0960-1481. doi: 10.1016/j.renene.2024.121391.
- M. Alday, F. Ardhuin, G. Dodet, and M. Accensi. Accuracy of numerical wave model results: application to the atlantic coasts of europe. *Ocean Sci.*, 18(6):1665–1689, 2022. doi: 10.5194/os-18-1665-2022.
- M. N. Allahdadi, B. Gunawan, J. Lai, R. He, and V. S. Neary. Development and validation of a regional-scale high-resolution unstructured model for wave energy resource characterization along the us east coast. *Renew. Energy*, 136:500–511, 2019. ISSN 0960-1481. doi: 10.1016/j.renene.2019.01.020.

R. Alonso and S. Solari. Automatic calibration and uncertainty quantification in waves dynamical downscaling. *Coast. Eng.*, 169:103944, 2021. ISSN 0378-3839. doi: 10.1016/j.coastaleng.2021.103944.

A. Apotsos, B. Raubenheimer, S. Elgar, and R. Guza. Testing and calibrating parametric wave transformation models on natural beaches. *Coast. Eng.*, 55(3):224–235, 2008. ISSN 0378-3839. doi: 10.1016/j.coastaleng.2007.10.002.

M. L. Banner, J. R. Gemmrich, and D. M. Farmer. Multiscale measurements of ocean wave breaking probability. *J. Phys. Oceanogr.*, 32(12):3364 – 3375, 2002. doi: 10.1175/1520-0485(2002)032<3364:MMOOWB>2.0.CO;2.

L. A. Bastidas, J. Knighton, and S. W. Kline. Parameter sensitivity and uncertainty analysis for a storm surge and wave model. *Nat. Hazards Earth Syst. Sci.*, 16(10):2195–2210, 2016. doi: 10.5194/nhess-16-2195-2016.

J. Battjes and J. P. F. M. Janssen. Energy loss and set-up due to breaking of random waves. *Coast. Eng.*, pages 569–587, 1978a. doi: 10.1061/9780872621909.034.

J. Battjes and J. P. F. M. Janssen. Energy loss and set-up due to breaking of random waves. In *Proceedings of the 16th International Conference on Coastal Engineering*, pages 569–587, 1978b.

J. Battjes and M. J. F. Stive. Calibration and verification of a dissipation model for random breaking waves. *Coast. Eng.*, 6(1):43–62, 1985. doi: 10.1016/0378-3839(85)90006-1.

M. Benoit, F. Marcos, and F. Becq. Development of a third-generation shallow water wave model with unstructured spatial meshing. In *Proceedings of the 25th International Conference on Coastal Engineering (ICCE)*, pages 465–478, Orlando, FL, USA, 1996. ASCE.

M. Benoit, F. Lafon, and G. Goasguen. Constitution et exploitation d'une base de données d'états de mer le long des côtes françaises par simulation numérique sur 23 ans. base anemoc en atlantique – manche – mer du nord. *Eur. J. Environ. Civ. En.*, 12/1-2:35–50, 2008.

J. Bergstra, R. Bardenet, Y. Bengio, and B. Kégl. Algorithms for hyper-parameter optimization. In J. Shawe-Taylor, R. Zemel, P. Bartlett, F. Pereira, and K. Weinberger, editors, *Advances in Neural Information Processing Systems*, volume 24. Curran Associates, Inc., 2011. Preprint at <https://inria.hal.science/hal-00642998v1/file/draft1.pdf>.

F. Bi, J. Song, K. Wu, and Y. Xu. Evaluation of the simulation capability of the wavewatch iii model for pacific ocean wave. *Acta Oceanol. Sin.*, 34(9):43–57, 2015. doi: 10.1007/s13131-015-0737-1.

J.-R. Bidlot, P. Janssen, and S. Abdalla. A revised formulation of ocean wave dissipation and its model impact. ECMWF Technical Memorandum 509, European Centre for Medium-Range Weather Forecasts (ECMWF), 2007.

M. Bitner-Gregersen, T. Waseda, J. Parunov, S. Yim, S. Hirdaris, N. Ma, and C. Guedes Soares. Uncertainties in long-term wave modelling. *Mar. Struct.*, 84:103217, 2022. ISSN 0951-8339. doi: 10.1016/j.marstruc.2022.103217.

E. Bouws and G. Komen. On the balance between growth and dissipation in an extreme depth-limited wind-sea in the southern north sea. *J. Phys. Oceanogr.*, 13(9):1653 – 1658, 1983. doi: 10.1175/1520-0485(1983)013<1653:OTBBGA>2.0.CO;2.

R. Campos, A. D'Agostini, B. França, A. Damiao, and C. Guedes Soares. Implementation of a multi-grid operational wave forecast in the south atlantic ocean. *Ocean Eng.*, 243:110173, 2022. ISSN 0029-8018. doi: 10.1016/j.oceaneng.2021.110173.

R. Carini, C. Chickadel, and A. Jessup. Surf zone waves at the onset of breaking: 2. predicting breaking and breaker type. *J. geophys. res. Ocean.*, 126:e2020JC016935, 2021. doi: 10.1029/2020JC016935.

M. Cialone and J. Smith. Wave transformation modeling with bottom friction applied to southeast oahu reefs. In *10th International Workshop on Wave Hindcasting and Forecasting & Coastal Hazard Assessment*, Vicksburg, MS, 2007. US Army Engineer Research and Development Center, Coastal and Hydraulics Laboratory.

H. Damlamian and J. Kruger. 2d coupled hydrodynamic spectral wave model of rangiroa – the 1983 orama–nisha tropical cyclone. Technical Report PR166, SPC Applied Geoscience and Technology Division (SOPAC), Suva, Fiji, 2013. Preprint at https://data-ww3.ifremer.fr/BIB/Damlamian_Kruger_SOPAC2013.pdf.

Deltas. *User Manual Calibration Instrument SWAN, Release 2.00.00*. Deltas, Delft, The Netherlands, 2009. Accessed via TU Delft Repository.

G. Dodet, J.-F. Piolle, Y. Quilfen, S. Abdalla, M. Accensi, F. Ardhuin, E. Ash, J.-R. Bidlot, C. Gommenginger, G. Marechal, M. Passaro, G. Quartly, J. Stopa, B. Timmermans, I. Young, P. Cipollini, and C. Donlon. The sea state cci dataset v1: towards a sea state climate data record based on satellite observations. *Earth Syst. Sci. Data*, 12(3):1929–1951, 2020. doi: 10.5194/essd-12-1929-2020.

J. Du, R. Bolaños, X. G. Larsén, and M. Kelly. Wave boundary layer model in swan revisited. *Ocean Sci.*, 15(2):361–377, 2019. doi: 10.5194/os-15-361-2019.

B. Dubarbier, B. Castelle, V. Marieu, and G. Ruessink. Process-based modeling of cross-shore sandbar behavior. *Coast. Eng.*, 95:35–50, 2015. ISSN 0378-3839. doi: 10.1016/j.coastaleng.2014.09.004.

C. Goeury, Y. Audouin, and F. Zaoui. Interoperability and computational framework for simulating open channel hydraulics: Application to sensitivity analysis and calibration of gironde estuary model. *Environ. Model. Softw.*, 148:105243, 2022. ISSN 1364-8152. doi: 10.1016/j.envsoft.2021.105243.

C. Goeury, T. Fouquet, T. Bagnis, M. Benoit, and M. Teles. Re-analysis of extreme sea state events modelling using a data-driven technique. In *8th IAHR Europe Congress*, Lisbon, Portugal, Jun 2024. International Association for hydro-Environment Engineering and Research. Preprint at <https://edf.hal.science/hal-04618518>.

C. J. Gon. Wave transformation on a rocky shoreline. Technical Report, Naval Postgraduate School, September 2019. Approved for public release; distribution is unlimited.

K. Hasselmann, T. Barnett, E. Bouws, H. Carlson, D. Cartwright, K. Enke, J. Ewing, H. Gienapp, D. Hasselmann, P. Kruseman, A. Meerburg, P. Müller, D. Olbers, K. Richter, W. Sell, and H. Walden. Measurements of wind-wave growth and swell decay during the joint north sea wave project (jonsswap), 1973.

S. Hasselmann and K. Hasselmann. Computations and parameterizations of the nonlinear energy transfer in a gravity-wave spectrum. part i: A new method for efficient computations of the exact nonlinear transfer integral. *J. Phys. Oceanogr.*, 15(11):1369–1377, 1985. doi: 10.1175/1520-0485(1985)015<1369:CAPOTN>2.0.CO;2.

J.-M. Hervouet. *Hydrodynamics of Free Surface Flows : Modelling with the finite element method*. Wiley, 2007. ISBN 978-0470035580.

P. A. E. M. Janssen. Quasi-linear theory of wind-wave generation applied to wave forecasting. *J. Phys. Oceanogr.*, 21(11):1631 – 1642, 1991. doi: 10.1175/1520-0485(1991)021<1631:QLTOWW>2.0.CO;2.

D. R. Jones, M. Schonlau, and W. J. Welch. Efficient global optimization of expensive black-box functions. *J. Glob. Optim.*, 13(4):455–492, 1998. doi: 10.1023/A:1008306431147.

M. Kalourazi, S. Siadatmousavi, A. Yeganeh-Bakhtiary, and F. Jose. Wavewatch-iii source terms evaluation for optimizing hurricane wave modeling: A case study of hurricane ivan. *Oceanologia*, 63(2):194–213, 2021. ISSN 0078-3234. doi: 10.1016/j.oceano.2020.12.001.

G. J. Komen, S. Hasselmann, and K. Hasselmann. On the existence of a fully developed wind-sea spectrum. *J. Phys. Oceanogr.*, 14(8):1271 – 1285, 1984. doi: 10.1175/1520-0485(1984)014<1271:OTECAF>2.0.CO;2.

N. Kraus and G. Kaminsky. Evaluation of depth-limited wave breaking criteria. In *Proceedings of the 2nd International Symposium on Ocean Wave Measurement and Analysis*, New York, NY, United States, 1994. American Society of Civil Engineers (ASCE).

A. Kroon, M. de Schipper, P. H. van Gelder, and S. G. Aarninkhof. Ranking uncertainty: Wave climate variability versus model uncertainty in probabilistic assessment of coastline change. *Coast. Eng.*, 158: 103673, 2020. ISSN 0378-3839. doi: 10.1016/j.coastaleng.2020.103673.

A. G. Majidi, V. Ramos, K. Amarouche, P. Rosa Santos, L. das Neves, and F. Taveira-Pinto. Assessing the impact of wave model calibration in the uncertainty of wave energy estimation. *Renew. Energy*, 212: 415–429, 2023. ISSN 0960-1481. doi: 10.1016/j.renene.2023.05.049.

K. Mouris, E. Espinoza, S. Schwindt, F. Mohammadi, S. Haun, S. Wiprecht, and S. Oladyshkin. Stability criteria for bayesian calibration of reservoir sedimentation models. *Model. Earth Syst. Environ.*, 9:3643–3661, 2023. doi: 10.1007/s40808-023-01712-7.

M. A. Mrozowska, J. Avery, A. Stoustrup, R. Nuterman, C.-J. Johnsen, A. Thormann, and M. Jochum. Bayesian optimization with gpu acceleration for ocean models. *J. geophys. res., Mach. learn. comput.*, 2 (3):e2024JH000517, 2025. doi: 10.1029/2024JH000517.

A. Nahon, D. Idier, N. Sénéchal, H. Féniès, C. Mallet, and J. Mugica. Imprints of wave climate and mean sea level variations in the dynamics of a coastal spit over the last 250 years: Cap ferret, sw france. *Earth Surf. Proc. Land.*, 44(11):2112–2125, 2019. doi: 10.1002/esp.4634.

N. Oreskes, K. Shrader-Frechette, and K. Belitz. Verification, validation, and confirmation of numerical models in the earth sciences. *Science*, 263(5147):641–646, 1994.

Y. Ozaki, Y. Tanigaki, S. Watanabe, M. Nomura, and M. Onishi. Multiobjective tree-structured parzen estimator. *J. Artif. Intell.*, 73:1209–1250, 04 2022. doi: 10.1613/jair.1.13188.

R. Padilla-Hernández and J. Monbaliu. Energy balance of wind waves as a function of the bottom friction formulation. *Coast. Eng.*, 43(2):131–148, 2001. doi: 10.1016/S0378-3839(01)00010-2.

I. Pairaud, F. Lyard, F. Auclair, T. Letellier, and P. Marsaleix. Dynamics of the semi-diurnal and quarter-diurnal internal tides in the bay of biscay. part 1: Barotropic tides. *Cont. Shelf Res.*, 28(10):1294–1315, 2008. ISSN 0278-4343. doi: 10.1016/j.csr.2008.03.004.

I. Pairaud, F. Auclair, P. Marsaleix, F. Lyard, and A. Pichon. Dynamics of the semi-diurnal and quarter-diurnal internal tides in the bay of biscay. part 2: Baroclinic tides. *Cont. Shelf Res.*, 30(3):253–269, 2010. ISSN 0278-4343. doi: 10.1016/j.csr.2009.10.008.

O. Phillips. *The Dynamics of the Upper Ocean*. Cambridge University Press, Cambridge, 2nd edition, 1977.

C. Raoult, A. Joly, M. Andreevsky, and A. Joly-Lauzel. ANEMOC-3: Improving the ANEMOC-2 sea state database by adding tide effects. In *Actes des 16èmes Journées de l'Hydrodynamique*, Marseille, France, 2018. 27–29 Novembre 2018.

W. Rattanapitikon and R. Karunchantadit. Comparison of dissipation models for irregular breaking waves. *Songklanakarin J. Sci. Technol.*, 24(1):139–148, 2002.

W. E. Rogers, J. M. Kaihatu, L. Hsu, R. E. Jensen, J. D. Dykes, and K. T. Holland. Forecasting and hindcasting waves with the swan model in the southern california bight. *Coast. Eng.*, 54(1):1–15, 2007. ISSN 0378-3839. doi: 10.1016/j.coastaleng.2006.06.011.

B. G. Ruessink. A bayesian estimation of parameter-induced uncertainty in a nearshore alongshore current model. *J. Hydroinformatics.*, 8(1):37–49, 01 2006. ISSN 1464-7141. doi: 10.2166/jh.2006.009.

J. Simmons, K. Splinter, M. Harley, and I. Turner. Calibration data requirements for modelling subaerial beach storm erosion. *Coast. Eng.*, 152:103507, 2019. ISSN 0378-3839. doi: 10.1016/j.coastaleng.2019.103507.

J. A. Simmons, M. D. Harley, L. A. Marshall, I. L. Turner, K. D. Splinter, and R. J. Cox. Calibrating and assessing uncertainty in coastal numerical models. *Coast. Eng.*, 125:28–41, 2017. ISSN 0378-3839. doi: 10.1016/j.coastaleng.2017.04.005.

S. Solari and R. Alonso. Automatic wave model calibration using surrogate models. In *Proceedings of the International Conference on Coastal Engineering (ICCE)*, number 37, Sep. 2022. doi: 10.9753/icce.v37.waves.43.

J. Song, L. Yu, W. Neiswanger, and S. Ermon. A general recipe for likelihood-free bayesian optimization. In *Proceedings of the 39th International Conference on Machine Learning (ICML)*, pages 20384–20404. PMLR, 2022.

A. H. Tanim, C. Smith-Lewis, A. R. Downey, J. Imran, and E. Goharian. Bayes_opt-swmm: A gaussian process-based bayesian optimization tool for real-time flood modeling with swmm. *Environ. Modell. Softw.*, 179:106122, 2024. ISSN 1364-8152. doi: 10.1016/j.envsoft.2024.106122.

J. C. Teixeira, M. P. Abreu, and C. Guedes Soares. Uncertainty of ocean wave hindcasts due to wind modeling. *J. Offshore Mech. Arct. Eng.*, 117(4):294–297, 11 1995. ISSN 0892-7219. doi: 10.1115/1.2827237.

M. Teles, M. Weiss, and M. Benoit. Assessment of the ANEMOC-3 sea state hindcast database for modelling a series of energetic winter storms along the french coast. In *XVIIèmes Journées Nationales Génie Côtier – Génie Civil*, pages 171–182, Chatou, France, 2022. doi: 10.5150/jngcgc.2022.019.

E. B. Thornton and R. T. Guza. Transformation of wave height distribution. *J. Geophys. Res. Oceans*, 88(C10):5925–5938, 1983. doi: 10.1029/JC088iC10p05925.

A. van der Westhuysen. Spectral modeling of wave dissipation on negative current gradients. *Coast. Eng.*, 68:17–30, 2012. ISSN 0378-3839. doi: 10.1016/j.coastaleng.2012.05.001.

A. van der Westhuysen, M. Zijlema, and J. Battjes. Nonlinear saturation-based whitecapping dissipation in swan for deep and shallow water. *Coast. Eng.*, 54:151–170, 2007. doi: 10.1016/j.coastaleng.2006.08.006.

A. J. van der Westhuysen. Modeling of depth-induced wave breaking under finite depth wave growth conditions. *J. Geophys. Res. Oceans*, 115(C1), 2010. doi: 10.1029/2009JC005433.

J. Vrugt and K. Beven. Embracing equifinality with uncertainty estimation: A review of glue, pest, and mcmc. *Environ. Model. Softw.*, 107:154–166, 2018. doi: 10.1016/j.envsoft.2018.06.001.

S. Watanabe. Tree-structured parzen estimator: Understanding its algorithm components and their roles for better empirical performance, 2023. Preprint at <https://arxiv.org/abs/2304.11127>.

A. Wurjanto, J. A. Mukhti, H. D. Wirasti, and Y. E. Widyanintias. Extreme significant wave height of western and central indonesian seas and its correlation with iso 19901-1:2015. *J. Eng. Technol. Sci.*, 52(3):331–342, 2020. doi: 10.5614/j.eng.technol.sci.2020.52.3.3.